PCCP

ROYAL SOCIETY OF CHEMISTRY

PAPER

View Article Online
View Journal | View Issue

Cite this: *Phys. Chem. Chem. Phys.*, 2021, **23**, 18517

Covalent photofunctionalization and electronic repair of 2H-MoS_2 *via* nitrogen incorporation†

Helena Osthues, [a] Christian Schwermann, [a] Johann A. Preuß, [b] Thorsten Deilmann, [a] Rudolf Bratschitsch, [b] Michael Rohlfing[a] and Nikos L. Doltsinis *[a]

Received 25th May 2021,
Accepted 13th August 2021

DOI: 10.1039/d1cp02313f

rsc.li/pccp

A route towards covalent functionalization of chemically inert 2H-MoS_2 exploiting sulfur vacancies is explored by means of (TD)DFT and GW/BSE calculations. Functionalization *via* nitrogen incorporation at sulfur vacancies is shown to result in more stable covalent binding than *via* thiol incorporation. In this way, defective monolayer MoS_2 is repaired and the quasiparticle band structure as well as the remarkable optical properties of pristine MoS_2 are restored. Hence, defect-free functionalization with various molecules is possible. Our results for covalently attached azobenzene, as a prominent photoswitch, pave the way to create photoresponsive two-dimensional (2D) materials.

1 Introduction

Molybdenum disulfide (MoS_2) and other transition metal dichalcogenides (TMDCs) have attracted widespread attention over the last decade in the field of two-dimensional (2D) materials. Similar to graphene, atomically thin sheets of the layered van der Waals crystals can be exfoliated mechanically, which, in the monolayer (ML) limit, possess a direct band gap and exhibit strong photoluminescence (PL), which is in the visible range for MoS_2.[1,2] TMDCs are therefore promising materials for potential applications in optoelectronic devices.[3,4]

Covalent chemical functionalization is critical to robustly tailor the electronic and optical properties of nanomaterials and to give them new functionalities required for various applications. MoS_2 in its stable semiconducting 2H-phase is chemically inert due to the lack of dangling bonds in the basal plane. Therefore sulfur vacancies, the predominant type of defect[5] in mechanically exfoliated and chemical vapor deposition (CVD) grown MoS_2 with the lowest formation energy,[6,7] are used as reactive centers for the attachment of nucleophilic functional groups, mostly thiols.[8–12] This yields a hypervalent structure as the sulfur atom of the deprotonated thiol-group fills the vacancy and binds to the three surrounding Mo atoms and the molecular rest. Recently, other protocols for covalent functionalization *via* carbon–sulfur-bonding were also developed.[13–15]

The reactivity of sulfur vacancies in MoS_2 has been long known and exploited to catalyze hydrodesulfurization,[16] and dissociation of the C–S bond at sulfur vacancies has been shown for different alkanethiols.[12,17,18] Elimination of defects is crucial to improve optical and transport properties of TMDCs. This has been achieved by treatment with acids[19,20] and thiol-containing molecules. The decomposition of thiol derivatives can be triggered by electrical stimulation[18] and thermal annealing[13,21,22] for the purpose of filling and repairing surface defects. However, theoretical investigations controversially debate the stability of the C–S bond.[23,24]

Amino acids have been shown to induce simultaneous exfoliation and covalent functionalization of 2H-MoS_2. XPS measurements and density functional theory (DFT) calculations suggest that the –NH groups bind at S-vacancies.[25,26]

Covalent functionalization using light-switchable molecules provides, for instance, the opportunity to interactively and reversibly alter the surface's electrical and optical properties. Azobenzene (AB) derivatives have been widely studied and applied in photoresponsive devices exploiting their light-induced isomerization accompanied by a pronounced change in molecular properties such as length or dipole moment.[27,28] Photo-tunable doping with proximal azobenzene derivatives alters the photoluminescence properties of monolayer MoS_2.[29]

In this work, *ab initio* calculations are performed to investigate the potential of nitrogen incorporation for defect-free functionalization of MoS_2. DFT binding energies are calculated to analyze the stability of the functionalized monolayer. Band structures and UV-vis absorption spectra based on the GW/BSE

[a] *Institute for Solid State Theory and Center for Multiscale Theory and Computation, Westfälische Wilhelms-Universität Münster, Wilhelm-Klemm-Str. 10, 48149 Münster, Germany. E-mail: nikos.doltsinis@wwu.de; Fax: +49 251 83 33669; Tel: +49 251 83 33582*

[b] *Institute of Physics and Center for Nanotechnology, Westfälische Wilhelms-Universität Münster, Wilhelm-Klemm-Str. 10, 48149 Münster, Germany*

† Electronic supplementary information (ESI) available: Computational details, graphical representation of binding energies, comparison of N/NH/NH_3 functionalization, MoS_2 + AB and MoS_2 + *cis*-AAB band structures and absorption spectrum. See DOI: 10.1039/d1cp02313f

approach within the LDA+GdW approximation[30,31] reveal the electronic and optical properties.

2 Computational details

2.1 Geometry optimizations

Geometry optimizations used an in-house modified version of CPMD 3.15.1[32] using a plane-wave basis with 70 Ry cutoff energy, the PBE density functional[33] and normconserving Goedecker–Teter–Hutter pseudopotentials.[34–36] van der Waals interactions were included by employing D3 dispersion correction with Becke–Johnson damping (BJ).[20,37–39] The 2D geometries in this work are calculated using hexagonal periodic boundary conditions with a 29 Å lattice constant vertical to the surface. The experimental value[40] of 3.16 Å was used for the MoS_2 lattice constant. The Brillouin zone was sampled by a Monkhorst–Pack mesh[41] of $9 \times 9 \times 1$ *k*-points and its equivalent for larger supercells. For example, for the 3×3 MoS_2 supercell a $3 \times 3 \times 1$ *k*-grid was used. Geometry optimizations were considered converged when all ionic forces were below 5×10^{-4} a.u. For potential energy bond scans, harmonic restraint potentials with a force constant of 3 a.u. were added to enforce a given bond length. Restrained geometry optimizations are carried out at the Γ-point using a 5×5 MoS_2 supercell, which is large enough to neglect interactions between molecules in neighboring unit cells. For large supercells, the energy discrepancy due to coarse *k*-sampling is small, especially for the energy differences calculated in this work.

2.2 GdW/BSE calculations

The DFT(LDA) eigenvalues and eigenvectors needed for the LDA+GdW calculations[30,31] were calculated using a basis of localized Gaussian orbitals (for detailed information see ESI†). Spin–orbit interaction was taken into account *via* norm conserving and separable pseudopotentials.[42–44] All band structure calculations employed a 3×3 MoS_2 supercell, *i.e.* a 9.48 Å × 9.48 Å × 29 Å cell. Quasiparticle energy calculations used a $6 \times 6 \times 1$ *k*-grid in the first Brillouin zone, which corresponds to a $18 \times 18 \times 1$ *k*-grid for a 1×1 MoS_2 unit cell, and an energy cutoff of the auxiliary plane wave basis of 2.5 Ry. The Bethe–Salpeter equation (BSE) was solved for four valence and six conduction bands and its equivalent for larger supercells. The exchange part of the electron–hole interaction kernel is calculated using a Gaussian basis set to handle the strongly localized molecular orbitals efficiently.

2.3 TDDFT calculations

For time-dependent DFT (TDDFT) calculations, the CP2K 6.1 program package[45] was utilized, which employs a mixed Gaussian and plane-wave basis set. A TZVP (DZVP-SR for Mo) basis set[46] and a plane-wave cutoff of 450 Ry were chosen together with the PBE functional. Optical spectra were computed *via* the linear-response (LR) TDDFT formalism in the Tamm–Dancoff approximation.[47] Absorption was calculated for a $6 \times 6 \times 1$ MoS_2 supercell at the Γ-point. All virtual orbitals were included in the calculation of the first 1000 excited states. An artificial Lorentzian function of 0.035 eV half-width is applied to the excitation energies to simulate the broadening in experimental measurements.

2.4 Visualisation

Molecular structures and orbitals were visualized using ADF 2018.206[48] and VMD.[49]

3 Results and discussion

3.1 Optimized geometries

Fig. 1 shows the optimized geometries of the systems we studied and compared. Although we consider low-energy structures in vacuum only, calculations of this type have proven valuable for predictions of measurements under realistic experimental conditions.[20,50] Most publications on the functionalization of the basal plane of 2H-MoS_2 (Fig. 1a) discuss bonding between a surface sulfur atom and a carbon atom of the attached molecule. Fig. 1d shows how MoS_2 can be functionalized with azobenzene in this way. In our work, an alternative linkage *via* Mo–N–C is studied, where a sulfur vacancy (Fig. 1b) is filled with a nitrogen atom, which binds not only to the three surrounding molybdenum atoms but additionally needs another single bond to be saturated. Saturation can be achieved with hydrogen (Fig. 1c), in the simplest case, or other molecules such as azobenzene (Fig. 1e and f).

In a pristine MoS_2 monolayer, the calculated Mo–S distance is 2.40 Å, which is in good agreement with experimentally measured value of 2.42 Å.[40] Attaching azobenzene to a sulfur atom leaves the position of Mo and S atoms almost unchanged. The C–S bond length is 1.81 Å. NH (Fig. 1c) binds to the three

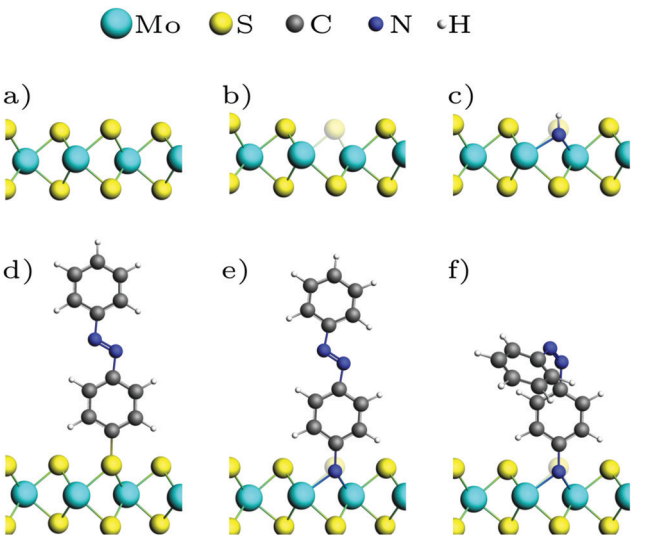

Fig. 1 Optimized geometries: (a) MoS_2 ML, (b) with sulfur vacancy, (c) with NH, (d) with *trans*-azobenzene (AB), (e) with *trans*-aminoazobenzene (AAB), (f) with *cis*-AAB in the vacancy. Note that the systems are fully periodic, for a top view see *e.g.* Fig. 3a.

neighboring Mo in equal distances of 2.10 Å in a vertical orientation to the basal plane. Replacing the hydrogen atom with azobenzene (Fig. 1e) slightly breaks the threefold symmetry, the N–Mo distances being 2.17 Å, 2.19 Å and 2.19 Å. The N–C bond is again oriented vertically, with a bond length of 1.46 Å, which is significantly larger than the 1.39 Å in the amino group of isolated aminoazobenzene (AAB), and almost as long as the C–N bond in methylamine with 1.48 Å, for example.

3.2 Binding energies

The binding energy for amino-containing molecules is calculated as follows:

$$E_b = -E_{ML(vac)} - E_{mol} + E_{ML+mol} + E_{H2} \quad (1)$$

where $E_{ML(vac)}$, E_{mol} and E_{ML+mol} are the total energies of the ML with a sulfur vacancy, the isolated molecule, and the functionalized monolayer, respectively. As two hydrogen atoms have to be removed from the amino group during the functionalization process, they are added to the product side as an isolated hydrogen molecule with total energy E_{H2}. To obtain a comparable value E_b for S–C-bonded molecules, the educts are a ML with a sulfur vacancy and a thiol-containing molecule. As only one hydrogen atom has to be removed from the thiol group, the binding energy is given by

$$E_b = -E_{ML(vac)} - E_{mol} + E_{ML+mol} + \frac{1}{2}E_{H_2}. \quad (2)$$

The sulfur vacancy can also be filled by oxygen.[20] Therefore, eqn (2) can be applied to hydroxy-containing molecules. In Table 1, the binding energies per molecule are reported for different chemical species (for a graphical representation of the corresponding chemical reaction including optimized geometries see Fig. S3–S9, ESI†). Both Mo–N and S–C type functionalizations are exothermic, as the Mo dangling bonds at the vacancy site are saturated.

Breaking the C–S bond in hypervalent functionalized systems gives pristine ML. The reaction energy for the repair of the sulfur vacancy can be calculated as

$$E_r = -E_{ML+mol} - \frac{1}{2}E_{H_2} + E_{ML} + E_{mol\text{-}thiol} \quad (3)$$

where E_{ML} is the total energy of the pristine ML, and $E_{mol\text{-}thiol}$ now is the molecule without the thiol group. For methanethiol the energy gain is −1.99 eV (see Fig. S10, ESI†) and for *p*-thioazobenzene it is −1.80 eV (see Fig. S11, ESI†). Hence, the repair mechanism for C–S type binding is exothermic,

Table 1 Binding energies E_b to a MoS_2 5 × 5 supercell

Molecule	Binding type	E_b (eV)
Methanethiol	C–S	−1.57
p-Thioazobenzene	C–S	−1.46
p-Hydroxyazobenzene	C–O	−0.24
Ammonia	Mo–N	−1.73
Methylamine	Mo–N	−2.03
p-Aminoazobenzene	Mo–N	−1.13
Glycine	Mo–N	−1.12

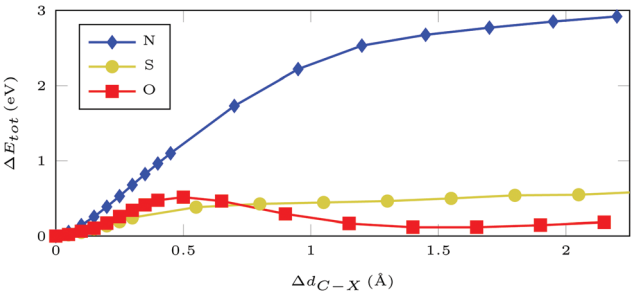

Fig. 2 Total DFT energy differences for a 5 × 5 MoS_2 supercell with AB attached at an atom of type X = (N/S/O) filling a sulfur vacancy. Geometries were optimized with restrained C–X distance.

which is in agreement with other published findings.[21,24] Similar behavior can be noted for binding *via* an oxygen atom within the sulfur vacancy. Breaking the C–O bond gives $E_r = -2.09$ eV for *p*-hydroxyazobenzene (see Fig. S12, ESI†).

Furthermore, we can probe the stability of the adsorbate with respect to rupture of the C–X bond, where X = (N, S, O) is the atom filling the sulfur vacancy, by potential hypersurface scans. For azobenzene bound *via* N, the energy rises steeply with increasing N–C distance, with the asymptotic limit being around 3 eV (Fig. 2). In contrast, hypervalent binding *via* sulfur or oxygen gives much flatter bond scans with maximum values of approximately 0.5 eV, *i.e.* thermodynamically accessible energy, which has been confirmed experimentally during thermal annealing.[13,21,22] Thus, functionalization *via* N results in much higher stability than functionalization *via* O or S. The main difference between bonding *via* the chalcogens or nitrogen is that, in the former case, there is an odd number of electrons which gives pristine ML and an azobenzene radical after bond breaking. For nitrogen bonding, which is described by an even number of electrons, removing the molecule results in two dangling bonds – both at the nitrogen, which is left within the ML, and at the molecular rest.

3.3 Electronic band structure

The DFT(LDA) band structures corresponding to the different functionalization types (Fig. 1) are calculated using a 3 × 3 MoS_2 ML supercell and the respective 2D surface Brillouin zone (Fig. 3a). In the LDA band structure of the pristine ML (Fig. 3b), there is a direct gap of 1.74 eV at $\bar{\Gamma}$, which contains (due to backfolding) the $\bar{K}$-point of the 1 × 1 unit cell. DFT(LDA) is known to underestimate the band gap, but as the dispersions are reproduced well in most cases, the DFT calculations can be used as a starting point for more accurate methods based on many-body perturbation theory.

Sulfur vacancies are the predominant type of defect in MoS_2.[5–7] If a sulfur atom is missing, defect states appear within the band gap (Fig. 3c) that are located at the sulfur vacancies.[50] In our calculation these states are not completely flat, which is due to interactions between neighboring vacancies. For one vacancy in each 3 × 3 supercell, the distance between neighboring defect sites is only 9.48 Å.

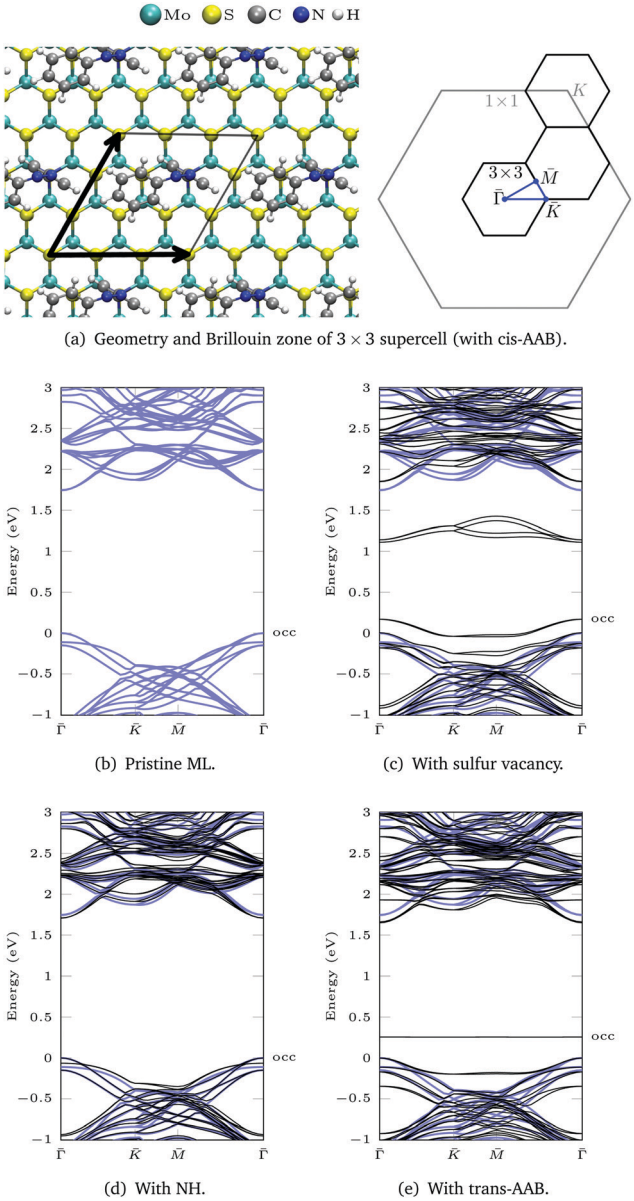

Fig. 3 (a) Geometry of a 3 × 3 supercell (with *cis*-AAB as an example) and the corresponding 2D Brillouin zone (BZ). (b)–(e) LDA band structures are calculated between the points of high symmetry (blue path in the BZ). The band structure of pristine ML is shown in blue. The valence band maximum of the ML is set to 0 eV to allow for better comparison. The highest occupied (occ) band of the functionalized system is labeled.

The dangling bonds at a sulfur vacancy can be saturated by inserting imino (NH) in the vacancy. Compared to the defective ML, the defect states disappear and the band structure deviates only slightly from pristine ML in the shown energy range (Fig. 3d). The type of bonding is similar for atomic nitrogen (compare geometries in Fig. S15 and charge density differences in Fig. S16, ESI†). Yet, in the deprotonated case there is a defect band above the ML valence bands in our DFT calculation (Fig. S17, ESI†), which can be exploited for p-type doping.[6,51,52] In contrast, NH_3 only weakly bonds to the surface[53] which is reflected by large Mo–N bond lengths (Fig. S15, ESI†) and multiple defect states within the MoS_2 band gap (Fig. S17, ESI†).

For AAB bound *via* Mo–N, the gap between the ML bands is reduced by 0.09 eV compared to the pristine ML (Fig. 3e). The main difference between MoS_2 functionalized with *trans*-AAB and *cis*-AAB can be found in the molecular orbitals (see the flat bands in Fig. 3e and Fig. S20, ESI†). In Fig. 4a, the band structures for the isolated molecules are compared with the functionalized ML. Orange points indicate the result of a Mulliken analysis,[54] their size reflecting to what extend the wave functions are located at the molecule. The valence band maximum (VBM) corresponds to the highest occupied molecular orbital (HOMO) of AAB which is mostly formed by electrons at the N=N double bond (Fig. S18, ESI†). The other molecular orbitals can also be identified in the band structure of the functionalized system.

Attaching AB to the ML *via* C–S bond introduces states within the band gap of the ML (Fig. S13, ESI†). These states are located at the C–S bond and the Mo atoms below as presented in the density isosurface plotted in Fig. S14 (ESI†). Detailed analysis of the band structure and calculated absorption of C–S functionalized MoS_2 can be found in the literature.[13,55–57] In this work, we focus on the electronic structure of MoS_2 functionalized by insertion of nitrogen into a sulfur vacancy.

Based on the DFT(LDA) calculations the GW method in the LDA+GdW approximation is employed to calculate the so-called quasiparticle corrections. In LDA+GdW calculations the HOMO–LUMO gap of isolated molecules increases. In the case of *trans*-AAB from 1.9 eV to 5.9 eV. In all calculations, the LDA+GdW Hamiltonian was diagonalized, therefore the final

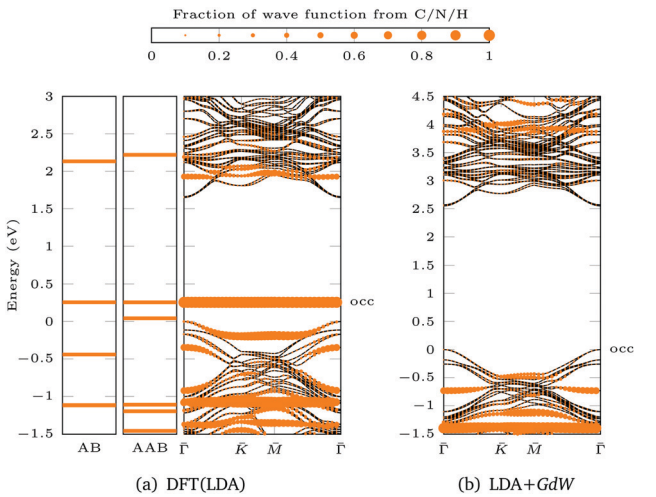

Fig. 4 Population analysis for *trans*-AAB-ML bandstructures in Fig. 3e and 5d: the size of the orange points is proportional to the part of the wave function stemming from C/N/H atoms. The valence band maximum of the ML is set to 0 eV. The highest occupied (occ) band of the functionalized system is labeled. (a) LDA band structures of AB (left), AAB (center) and *trans*-AAB-ML (right). (b) LDA+GdW band structures of *trans*-AAB-ML. Note the different energy scales.

quasiparticle wave functions are linear combinations of the DFT wave functions. This is important as the molecular and ML orbitals are hybridized and the quasiparticle corrections are different for molecular and MoS_2 states. The hybridization hinders the determination of the energy difference between HOMO and lowest unoccupied molecular orbital (LUMO) for the *trans*-AAB-ML system (Fig. 4b). The HOMO is roughly 0.5 eV lower in energy than the ML VBM, and the LUMO is at around 3 eV. Hence, the HOMO–LUMO gap is smaller than the gap of the isolated molecule, which is due to the screening of the ML. The molecule itself increases the polarizability of the environment surrounding the ML and hence the band gap is reduced by 0.2 eV compared to the pristine ML (Fig. 5a and d). The gap is 0.03 eV lower if the bound AAB changes from *trans* to *cis* configuration (Fig. S21, ESI†). For MoS_2, the band dispersion is reproduced reasonably well in LDA, but the band gap of the ML increases from 1.74 eV in LDA to 2.73 eV in LDA+GdW.‡ This is roughly four times less pronounced compared to the AAB states, because in the ML additional charges can be screened more efficiently by polarization of the surrounding electron density.

For the ML with vacancy (Fig. 5b) and NH-functionalization (Fig. 5c) a similar band gap widening can be noted.

3.4 Optical properties

Fig. 6 shows the absorption spectra calculated using GdW/BSE. The pristine MoS_2 ML has two characteristic spin–orbit-split absorption peaks, A and B, at 2.13 eV and 2.29 eV. If one sulfur atom is missing, there are multiple peaks at lower energies. For larger supercells, *i.e.* larger distances between two vacancies, these excitations converge to one absorption peak at approximately 1.8 eV.[58] They can be attributed to transitions into the defect states within the band gap. Filling the vacancy with NH repairs the defects and low-lying transitions disappear. The excitations are slightly broadened and shifted by approximately −0.03 eV (8 nm) compared to pristine ML. If the ML is functionalized with AAB, all peaks are broadened. The energy shift for the A exciton is −0.04 eV compared to pristine MoS_2. In the shown energy range there is only one transition originating from the molecular HOMO. It is located at 2.00 eV with very small oscillator strength, which can be identified as the HOMO–LUMO excitation of (amino-)azobenzene. The excitation energy is significantly smaller than the experimental value, which is roughly 2.7 eV.[59] The difference is mostly due to the small unit cell. For gas-phase AAB in a 3 × 3 supercell (without Mo and S atoms), the first excited state of the molecule is at 2.14 eV. For *cis*-AAB binding to the surface decreases the energy of the HOMO–LUMO excitation by 0.21 eV. A thorough investigation of this effect requires a larger supercell, but it is computationally extremely demanding to study the intramolecular transitions for this system, as a vast number of MoS_2-type bands have to be included to take into account a sufficient number of AAB-type bands. This problem is exacerbated for larger supercells.

Isomerization in AB derivatives proceeds *via* excited electronic states, therefore these states have to be analyzed in detail in order to probe the switchability of AB derivatives attached

‡ As polarisation effects are included in LDA+GdW more vacuum is needed between the layers to exactly calculate the band gap. The gap is approximately 0.2 eV larger for infinite interlayer distance, *i.e.* 2.9 eV.[31]

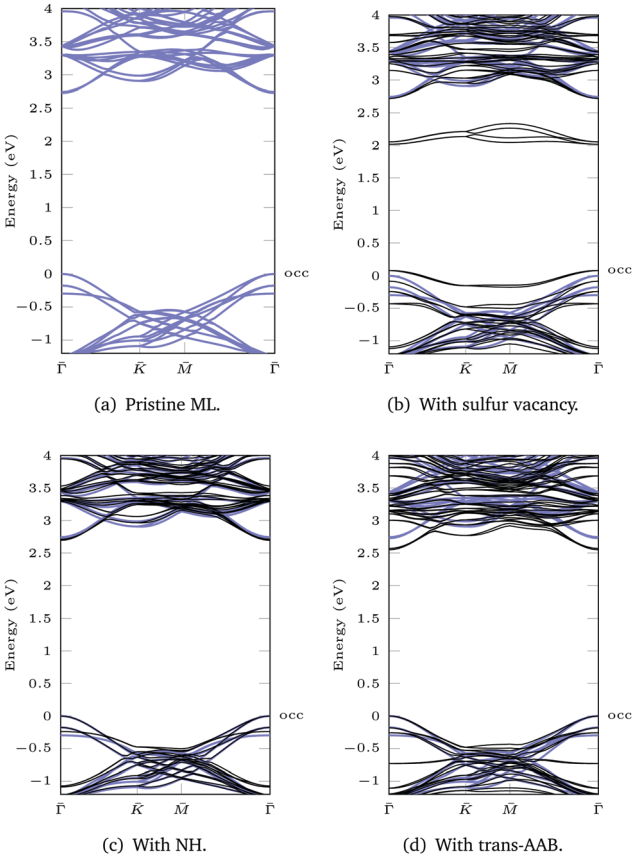

Fig. 5 LDA+GdW band structures for 3 × 3 supercells. The pristine ML is shown in blue. The valence band maximum of the ML is set to 0 eV to allow for better comparison. The highest occupied (occ) band of the functionalized system is labeled.

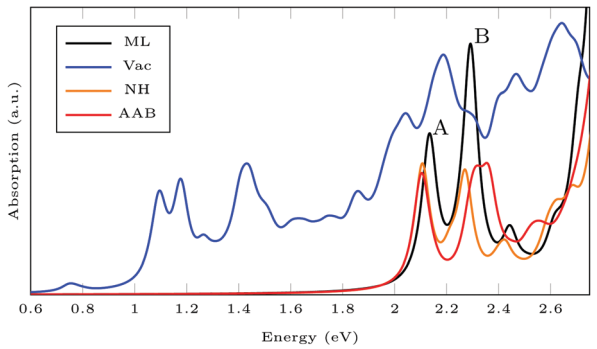

Fig. 6 Exciton absorption spectrum (GdW/BSE) of pristine MoS_2 monolayer (ML), with sulfur vacancy (Vac), NH and *trans*-aminoazobenzene (AAB) in a vacancy.

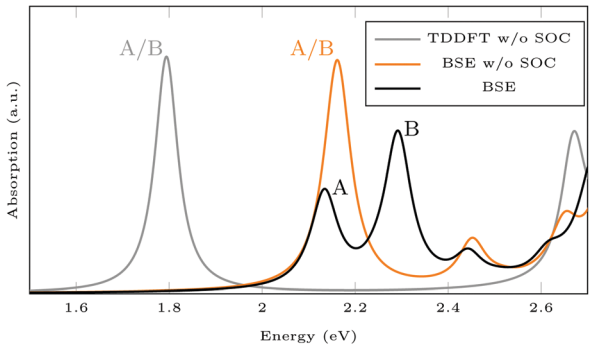

Fig. 7 Absorption spectra calculated using GdW/BSE and TDDFT. The splitting into A and B exciton is due to spin–orbit coupling (SOC).

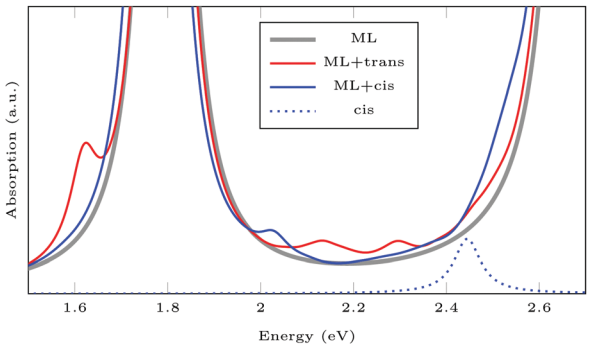

Fig. 8 TDDFT spectra of pristine ML, and of MLs functionalized with AAB in *trans* and *cis* configuration. Absorption of isolated *cis*-AAB is shown for comparison. *trans*-AAB is not shown, as the excitation at 2.32 eV has very small oscillator strength.

to MoS_2. Since they are based on two-point functions only, LR-TDDFT calculations in the adiabatic approximation are less costly and analytical nuclear forces are widely available. TDDFT with GGA functionals is known to underestimate excitation energies in semiconducting solids,[60] but here, we focus on the influence of the covalently bound surface on the intramolecular excitations. Spin–orbit coupling (SOC) is neglected to further reduce the computational effort. The splitting into A and B exciton is due to SOC as one can see when comparing the BSE results with and without SOC (see Fig. 7). The energy for the first excitation(s) is too high in BSE, whereas it is too low in TDDFT, compared to the experimental value of about 1.97 eV.[61] In both BSE and TDDFT, this excitation is a transition from the valence band maximum with Mo-d_{xy}/$d_{x^2-y^2}$ type to the conduction band minimum with Mo-d_{z^2} type.

For isolated AAB, the lowest TDDFT excitations are at 2.33 eV and 2.45 eV for *trans* and *cis*, respectively. The AAB-functionalized ML shows additional peaks compared to pristine MoS_2 (see Fig. 8). For ML + *trans*-AAB the intramolecular HOMO–LUMO transition can be identified at 2.33 eV. The absorption spectrum is very similar to the pristine ML, but there is an additional peak at 1.62 eV, which is an excitation from the molecular HOMO−1 to the lowest MoS_2 state. This excitation energy from molecule to ML is likely to be underestimated as TDDFT with GGA functional PBE struggles with charge transfer excitations.§ For ML + *cis*-AAB the HOMO–LUMO excitation energy cannot be determined exactly as hybridization of the LUMO with MoS_2 conduction bands splits the excitation into many transitions with different energies. The small peak at 2.0 eV is a charge transfer excitation from molecule to ML.

The analysis of the TDDFT spectra reveals two challenges for *ab initio* simulations of the first excited intramolecular excitation: (1) hybridization makes it difficult to identify the excitation of interest and treat it separately. (2) Errors in the ordering of excited potential energy surfaces falsifies excited states molecular dynamics when using GGA functionals.

§ Unfortunately, the use of (range-separated) hydrid functionals is computationally prohibitive in this case.

4 Conclusions

We have demonstrated defect-free functionalization of MoS_2 *via* incorporation of nitrogen atoms at sulfur vacancies. Increased stability of N–Mo bound azobenzene as opposed to common C–S bonding is demonstrated by DFT calculations. Defect states within the band gap of monolayer MoS_2 are removed by our functionalization approach. This is verified by LDA+GdW band structure calculations. Photoabsorption of functionalized MoS_2 resembles that of pristine ML as shown by GdW/BSE. Hence, our work shows that MoS_2 can be functionalized while keeping its remarkable properties. Stable attachment of azobenzene derivatives is the key to photoresponsive 2D materials with exciting optical properties.

In this work, we solely focus on point defects. For other types of defects,[62–66] restoring the electronic band structure of pristine MoS_2 by functionalization is more challenging and will be the subject of future studies.

As far as the photoswitchability of covalently attached AAB on MoS_2 is concerned, theoretical treatment within LR-TDDFT faces the problem that, due to mixing between molecular and substrate orbitals, it is impossible to single out one particular excited state in which photoisomerization proceeds. An investigation of switching efficiency would thus require a nonadiabatic dynamical treatment taking into account a large manifold of excited states. Due to the charge transfer character of many relevant states, a hybrid functional (possibly range-separated) would have to be used to ensure the correct state ordering. All in all, this would, however, entail an enormous computational cost.

Conflicts of interest

There are no conflicts to declare.

Acknowledgements

H. O. and J. A. P. gratefully acknowledge the Graduate School of Molecules and Interfaces WWU Münster for financial support. T. D. acknowledges financial support from the German Research Foundation (DFG Projects No. DE 2749/2-1). The

authors also thank T. Stiehm, R. Schmidt, R. Schneider, J. Kern, and S. Michaelis de Vasconcellos for fruitful discussions. The computations were carried out using resources provided by the ZIV of the University of Münster (PALMA II HPC cluster).

Notes and references

1 K. F. Mak, C. Lee, J. Hone, J. Shan and T. F. Heinz, *Phys. Rev. Lett.*, 2010, **105**, 136805.
2 A. Splendiani, L. Sun, Y. Zhang, T. Li, J. Kim, C.-Y. Chim, G. Galli and F. Wang, *Nano Lett.*, 2010, **10**, 1271.
3 K. F. Mak and J. Shan, *Nat. Photonics*, 2016, **10**, 216.
4 Q. H. Wang, K. Kalantar-Zadeh, A. Kis, J. N. Coleman and M. S. Strano, *Nat. Nanotechnol.*, 2012, **7**, 699.
5 J. Hong, Z. Hu, M. Probert, K. Li, D. Lv, X. Yang, L. Gu, N. Mao, Q. Feng and L. Xie, *et al.*, *Nat. Commun.*, 2015, **6**, 6293.
6 H.-P. Komsa, J. Kotakoski, S. Kurasch, O. Lehtinen, U. Kaiser and A. V. Krasheninnikov, *Phys. Rev. Lett.*, 2012, **109**, 035503.
7 W. Zhou, X. Zou, S. Najmaei, Z. Liu, Y. Shi, J. Kong, J. Lou, P. M. Ajayan, B. I. Yakobson and J.-C. Idrobo, *Nano Lett.*, 2013, **13**, 2615.
8 S. S. Chou, M. De, J. Kim, S. Byun, C. Dykstra, J. Yu, J. Huang and V. P. Dravid, *J. Am. Chem. Soc.*, 2013, **135**, 4584.
9 D. M. Sim, M. Kim, S. Yim, M.-J. Choi, J. Choi, S. Yoo and Y. S. Jung, *ACS Nano*, 2015, **9**, 12115.
10 K. Cho, M. Min, T.-Y. Kim, H. Jeong, J. Pak, J.-K. Kim, J. Jang, S. J. Yun, Y. H. Lee and W.-K. Hong, *et al.*, *ACS Nano*, 2015, **9**, 8044.
11 S. Bertolazzi, S. Bonacchi, G. Nan, A. Pershin, D. Beljonne and P. Samor, *Adv. Mater.*, 2017, **29**, 1606760.
12 S. Bertolazzi, M. Gobbi, Y. Zhao, C. Backes and P. Samor, *Chem. Soc. Rev.*, 2018, **47**, 6845.
13 X. S. Chu, A. Yousaf, D. O. Li, A. A. Tang, A. Debnath, D. Ma, A. A. Green, E. J. Santos and Q. H. Wang, *Chem. Mater.*, 2018, **30**, 2112.
14 M. Vera-Hidalgo, E. Giovanelli, C. Navo and E. M. Pérez, *J. Am. Chem. Soc.*, 2018, **141**, 3767.
15 R. Quirós-Ovies, M. Vázquez Sulleiro, M. Vera-Hidalgo, J. Prieto, I. J. Gómez, V. Sebastián, J. Santamara and E. M. Pérez, *Chem. – Eur. J.*, 2020, **26**, 6629.
16 A. Aoshima and H. Wise, *J. Catal.*, 1974, **34**, 145.
17 S. L. Peterson and K. H. Schulz, *Langmuir*, 1996, **12**, 941.
18 M. Makarova, Y. Okawa and M. Aono, *J. Phys. Chem. C*, 2012, **116**, 22411.
19 M. Amani, D.-H. Lien, D. Kiriya, J. Xiao, A. Azcatl, J. Noh, S. R. Madhvapathy, R. Addou, K. Santosh and M. Dubey, *et al.*, *Science*, 2015, **350**, 1065.
20 C. Schwermann, T. Stiehm, P. Tonndorf, R. Schneider, R. Schmidt, J. Kern, S. M. de Vasconcellos, R. Bratschitsch and N. Doltsinis, *Phys. Chem. Chem. Phys.*, 2018, **20**, 16918.
21 Z. Yu, Y. Pan, Y. Shen, Z. Wang, Z.-Y. Ong, T. Xu, R. Xin, L. Pan, B. Wang and L. Sun, *et al.*, *Nat. Commun.*, 2014, **5**, 5290.
22 Y. Park, S. Shin, Y. An, J.-G. Ahn, G. Shin, C. Ahn, J. Bang, J. Baik, Y. Kim and J. Jung, *et al.*, *ACS Appl. Mater. Interfaces*, 2020, **12**, 40870.
23 Q. Li, Y. Zhao, C. Ling, S. Yuan, Q. Chen and J. Wang, *Angew. Chem., Int. Ed.*, 2017, **56**, 10501.
24 A. Förster, S. Gemming, G. Seifert and D. Tománek, *ACS Nano*, 2017, **11**, 9989.
25 E. Satheeshkumar, A. Bandyopadhyay, M. Sreedhara, S. K. Pati, C. Rao and M. Yoshimura, *ChemNanoMat*, 2017, **3**, 172.
26 S. Kumari, A. Chouhan, O. P. Sharma, S. Kuriakose, S. A. Tawfik, M. J. Spencer, S. Walia, H. Sugimura and O. P. Khatri, *ACS Appl. Mater. Interfaces*, 2020, **12**, 30720.
27 *Molecular Switches*, ed. B. L. Feringa and R. W. Browne, Wiley-VCH, Weinheim, 2011.
28 *Smart Light-Responsive Materials: Azobenzene-Containing Polymers and Liquid Crystals*, ed. Y. Zhao and T. Ikeda, Wiley-VCH, Weinheim, 2009.
29 J. Li, J. Wierzbowski, Ö. Ceylan, J. Klein, F. Nisic, T. L. Anh, F. Meggendorfer, C.-A. Palma, C. Dragonetti and J. V. Barth, *et al.*, *Appl. Phys. Lett.*, 2014, **105**, 241116.
30 M. Rohlfing, *Phys. Rev. B: Condens. Matter Mater. Phys.*, 2010, **82**, 205127.
31 M. Drüppel, T. Deilmann, J. Noky, P. Marauhn, P. Krüger and M. Rohlfing, *Phys. Rev. B*, 2018, **98**, 155433.
32 CPMD, http://www.cpmd.org/, Copyright IBM Corp 1990–2015, Copyright MPI für Festkörperforschung Stuttgart 1997–2001.
33 J. P. Perdew, K. Burke and M. Ernzerhof, *Phys. Rev. Lett.*, 1996, **77**, 3865.
34 S. Goedecker, M. Teter and J. Hutter, *Phys. Rev. B: Condens. Matter Mater. Phys.*, 1996, **54**, 1703.
35 C. Hartwigsen, S. Gœdecker and J. Hutter, *Phys. Rev. B: Condens. Matter Mater. Phys.*, 1998, **58**, 3641.
36 M. Krack, *Theor. Chem. Acc.*, 2005, **114**, 145.
37 S. Grimme, J. Antony, S. Ehrlich and H. Krieg, *J. Chem. Phys.*, 2010, **132**, 154104.
38 S. Grimme, S. Ehrlich and L. Goerigk, *J. Comput. Chem.*, 2011, **32**, 1456.
39 D. G. Smith, L. A. Burns, K. Patkowski and C. D. Sherrill, *J. Phys. Chem. Lett.*, 2016, **7**, 2197.
40 T. Böker, R. Severin, A. Müller, C. Janowitz, R. Manzke, D. Voß, P. Krüger, A. Mazur and J. Pollmann, *Phys. Rev. B: Condens. Matter Mater. Phys.*, 2001, **64**, 235305.
41 H. J. Monkhorst and J. D. Pack, *Phys. Rev. B: Solid State*, 1976, **13**, 5188.
42 L. Kleinman and D. Bylander, *Phys. Rev. Lett.*, 1982, **48**, 1425.
43 D. Hamann, *Phys. Rev. B: Condens. Matter Mater. Phys.*, 1989, **40**, 2980.
44 L. Hemstreet, C. Fong and J. Nelson, *Phys. Rev. B: Condens. Matter Mater. Phys.*, 1993, **47**, 4238.
45 CP2K version 6.1, the CP2K developers group, 2018, CP2K is freely available from https://www.cp2k.org/.
46 J. VandeVondele and J. Hutter, *J. Chem. Phys.*, 2007, **127**, 114105.
47 M. E. Casida, *THEOCHEM*, 2009, **914**, 3.

48 G. te Velde, F. M. Bickelhaupt, E. J. Baerends, C. Fonseca Guerra, S. J. van Gisbergen, J. G. Snijders and T. Ziegler, *J. Comput. Chem.*, 2001, **22**, 931.
49 W. Humphrey, A. Dalke and K. Schulten, *J. Mol. Graphics*, 1996, **14**, 33.
50 S. W. Han, G.-B. Cha, K. Kim and S. C. Hong, *Phys. Chem. Chem. Phys.*, 2019, **21**, 15302.
51 A. Azcatl, X. Qin, A. Prakash, C. Zhang, L. Cheng, Q. Wang, N. Lu, M. J. Kim, J. Kim and K. Cho, *et al.*, *Nano Lett.*, 2016, **16**, 5437.
52 C. Hu, C. Yuan, A. Hong, M. Guo, T. Yu and X. Luo, *Appl. Phys. Lett.*, 2018, **113**, 041602.
53 H. Li, M. Huang and G. Cao, *Phys. Chem. Chem. Phys.*, 2016, **18**, 15110.
54 R. S. Mulliken, *J. Chem. Phys.*, 1955, **23**, 1833.
55 L. Gao, Z.-D. Yang and G. Zhang, *Chem. Phys.*, 2017, **490**, 29.
56 M. Palummo, A. D'Auria, J. Grossman and G. Cicero, *J. Phys.: Condens. Matter*, 2019, **31**, 235701.
57 L. O. Jones, M. A. Mosquera, M. A. Ratner and G. C. Schatz, *ACS Appl. Mater. Interfaces*, 2020, **12**, 4607.
58 M. Drüppel, PhD thesis, University of Münster, 2017.
59 Y. Hirose, H. Yui and T. Sawada, *J. Phys. Chem. A*, 2002, **106**, 3067.
60 N. T. Maitra, *J. Chem. Phys.*, 2016, **144**, 220901.
61 A. Arora, N. K. Wessling, T. Deilmann, T. Reichenauer, P. Steeger, P. Kossacki, M. Potemski, S. M. de Vasconcellos, M. Rohlfing and R. Bratschitsch, *Phys. Rev. B*, 2020, **101**, 241413.
62 E. Mitterreiter, *et al.*, *Nat. Commun.*, 2021, **12**, 3822.
63 F. Bertoldo, *et al.*, *ACS Nano*, 2021, **15**, 2858.
64 W. Liao, K. Xie, L. Liu, X. Wang, Y. Luo, S. Liang, F. Liu and L. Jiang, *J. Energy Chem.*, 2021, **62**, 359.
65 J.-A. Ke, S. Garaj and S. Gradečak, *ACS Appl. Mater. Interfaces*, 2019, **11**, 26228.
66 J. Xie, *et al.*, *Adv. Mater.*, 2013, **85**, 5807.

